$Bi_{13}S_{18}X_2$-Based Solar Cells (X = Cl, Br, I): Photoelectric Behavior and Photovoltaic Performance

Sen Li,[1] Linfeng Xu,[2] Xinggang Kong,[3] Takafumi Kusunose,[1] Noriaki Tsurumachi,[1] and Qi Feng[1,*]

[1] *Department of Advanced Materials Science, Faculty of Engineering and Design, Kagawa University, 2217-20 Hayashi-cho, Takamatsu 761-0396, Japan*

[2] *Institute of Environment-friendly Materials and Occupational Health (Wuhu) and School of Earth and Environment, Anhui University of Science and Technology, Huainan, Anhui 241000, China*

[3] *School of Materials Science and Engineering, Shaanxi University of Science and Technology, Weiyang, Xi'an, Shaanxi, 710021, PR China*

(Received 9 September 2020; revised 17 January 2021; accepted 9 February 2021; published 15 March 2021)

Bismuth chalcohalides of $Bi_{13}S_{18}X_2$ (X = Cl, Br, I) are solvothermally synthesized and systematically characterized as a light absorber for photovoltaics. Rietveld refinements reveal that $Bi_{13}S_{18}X_2$ compounds adopt the same hexagonal structure with space group $P3$ and a chemical composition of $(Bi^{3+})_{12}(Bi_2^{4+})_{0.5}(S^{2-})_{18}(X^-)_2$, where a triangular tunnel is constructed from $[Bi_4S_6]$-ribbon spokes in the c-axial direction, X^- is located in the tunnel sites, and Bi(II) dimers of (Bi_2^{4+}) are located at the hexagonal center. The photoelectric behavior is investigated using ultraviolet-to-visible-to-near-infrared (UV-vis-NIR) absorption spectroscopy, ultraviolet photoelectron spectroscopy, x-ray photoelectron spectroscopy, Mott-Schottky plots, and conductivity measurements. The $Bi_{13}S_{18}X_2$ compounds are indirect n-type semiconductors with narrow band gaps of 0.76, 0.80, and 0.81 eV for $Bi_{13}S_{18}Cl_2$, $Bi_{13}S_{18}Br_2$, and $Bi_{13}S_{18}I_2$, respectively, and exhibit strong light absorbance over a wide wavelength range from UV to NIR. A facile physical vapor deposition approach is developed for the fabrication of a homogeneous $Bi_{13}S_{18}X_2$ thin film to study the photovoltaic performances. Solar cells with the architecture fluorine-doped tin oxide/TiO_2/$Bi_{13}S_{18}X_2$/(I_3^-/I^- redox couple)/Pt demonstrate power conversion efficiencies of 0.91, 1.12, and 0.75% for $Bi_{13}S_{18}Cl_2$, $Bi_{13}S_{18}Br_2$, and $Bi_{13}S_{18}I_2$, respectively. The highest cell performance of $Bi_{13}S_{18}Br_2$ can be attributed to its higher light-absorption ability.

DOI: 10.1103/PhysRevApplied.15.034040

I. INTRODUCTION

Recently, binary, ternary, and quaternary compounds of nontoxic elements have become the protagonists for the development of photoelectric materials [1]. Bismuth is a nontoxic element and a relatively low-price element due to its abundance in the earth's crust [2–5]. Among the bismuth-based ternary compounds, Bi-VI-VII compounds evoke enormous interest as functional electronic materials, owing to their interesting photoelectric, electromechanical, electro-optical, ferroelectric, piezoelectric, and electromechanical properties, and a large temperature dependence of the band gap [6–9]. Bismuth oxyhalides [BiOX, where X = Cl, Br, I], possessing a layered structure, attract much attention as visible-light-response photocatalysts [10–13]. Furthermore, the band gaps of their solid solutions, such as $BiOBr_xI_{1-x}$, can be changed continually with changing chemical compositions [14,15]. Bismuth chalcogenide halides BiSX, where X = Cl, Br, I] have great potential applications in visible-light-response photocatalysts and photovoltaics due to their attractive photoelectric performance [7,16,17]. BiSeX (X = Cl, Br, I) compounds exhibit a photoelectric response in the region from the visible to near-infrared wavelength, suggesting the possibility of photovoltaic applications [18–20].

The Bi-VI-VII compounds are promising light-absorber materials for photovoltaics because their properties are similar to those of lead-based halide perovskites, i.e., Bi(III) and Pb(II) have the same stable electronic configuration of $d^{10}s^2p^0$, similar ionic radii, and similar electronegativities [18]. In this sense, Bi-VI-VII compounds are expected to be alternatives to lead-based halide perovskites as photovoltaic materials to solve the toxicity and unstable problems of lead-based halide perovskites in the perovskite solar cells. In the Bi-VI-VII compounds, $Bi_{13}S_{18}X_2$ (X = Cl, Br, I) compounds are one of the most promising photovoltaic materials due to their broad photoelectric responses in the region from the visible to near-infrared wavelength. However, only limited studies have been reported on $Bi_{13}S_{18}X_2$ compounds

*feng.qi@kagawa-u.ac.jp

because stoichiometric $Bi_{13}S_{18}X_2$ compounds are difficult to synthesize.

Traditionally, bismuth chalcohalides are synthesized using a vapor-transport process and a flux process under high-temperature conditions over 600 °C [21–24]. Recently, the syntheses of $Bi_{13}S_{18}X_2$ by employing solution processes have been reported. $Bi_{13}S_{18}I_2$ can be synthesized by a solvothermal process [25–27]. $Bi_{13}S_{18}Br_2$ can be synthesized by hydrothermal and solvothermal processes [28,29]. $Bi_{13}S_{18}Cl_2$ can also be obtained by using a solvothermal route [30]. There is some debate about the structures and chemical compositions of $Bi_{13}S_{18}X_2$ compounds. Miehe and Kupčík reported a study on a $Bi_{13}S_{18}I_2$ compound in 1971 and concluded that it belonged to the hexagonal crystal system with the $P6_3$ space group and a chemical formula of $Bi(Bi_2S_3)_9I_3$ [31]. Other studies reported that the $Bi_{13}S_{18}I_2$ compound belonged to the hexagonal system with $P6_3/m$ or $P6_3$ space groups and chemical formulas of $Bi_{19}S_{27}I_3$ or $[Bi(Bi_2S_3)_9I_3]_{2/3}$ [21, 32,33]. Recently, Groom *et al.* rediscovered the $Bi_{13}S_{18}I_2$ structure by single-crystal XRD and powder synchrotron XRD, resulting in a stoichiometry of $Bi_{13}S_{18}I_2$ with the $P3$ space group due to the formation of a bivalent Bi(II) dimer of Bi_2^{4+} in this compound [22]. Fewer studies reported on $Bi_{13}S_{18}Br_2$ and $Bi_{13}S_{18}Cl_2$ compounds than that on $Bi_{13}S_{18}I_2$. These studies commonly resulted in the hexagonal crystal system with the $P6_3$ space group and chemical formulas of $Bi_{19}S_{27}Br_3$ and $Bi_{19}S_{27}Cl_3$, where all Bi are trivalence [23,24,29,34]. Although the formations of the Bi(II) dimer of Bi_2^{4+} in $Bi_{13}S_{18}Br_2$ and $Bi_{13}S_{18}Cl_2$ are also possibly similar to $Bi_{13}S_{18}I_2$, but it is unclear [22].

Another argument about $Bi_{13}S_{18}X_2$ is that it is a direct semiconductor or an indirect semiconductor [21,22]. Yan *et al.* reported that $Bi_{13}S_{18}I_2$ showed a direct transition band gap of 0.83 eV [25]. However, Groom *et al.* reported an indirect transition band gap of 0.82 eV for $Bi_{13}S_{18}I_2$ [22]. It has been reported that $Bi_{13}S_{18}Cl_2$ and $Bi_{13}S_{18}Br_2$ are direct semiconductors with band gaps of 1.6 and 1.42 eV, respectively [28,30]. Photoelectric studies reveal that $Bi_{13}S_{18}I_2$ demonstrates a broad photoelectric response, ranging from ultraviolet to near-infrared wavelength and can be applied as a light absorber in a photodetector device with high stability and reproducibility [25,26]. Very recently, we reported a study on a $Bi_{13}S_{18}I_2$-based solar cell creatively fabricated by a solution process, demonstrating a power conversion efficiency (PCE) of 0.85% [27]. Only a few studies have reported on the photoelectric behavior of $Bi_{13}S_{18}Br_2$ and $Bi_{13}S_{18}Cl_2$ based on their visible-light-response photocatalytic performances [28–30]. No study has been reported on $Bi_{13}S_{18}Br_2$- and $Bi_{13}S_{18}Cl_2$-based solar cells.

As described above, a detailed study on the photoelectric behavior of $Bi_{13}S_{18}X_2$ ($X = Cl, Br, I$) is necessary for the applications of $Bi_{13}S_{18}X_2$ compounds to photovoltaic and other photoelectric materials. In the present study, we develop solvothermal processes for the syntheses of $Bi_{13}S_{18}Cl_2$ and $Bi_{13}S_{18}Br_2$ and systematically characterize the photoelectric behavior of $Bi_{13}S_{18}X_2$ as light absorbers for solar cells. We provide evidence that $Bi_{13}S_{18}Cl_2$ and $Bi_{13}S_{18}Br_2$ adopt similar structures to that of $Bi_{13}S_{18}I_2$ with the $P3$ space group and a chemical formula of $Bi_{13}S_{18}X_2$, rather than the previously reported $P6_3$ space group and chemical formula of $Bi_{19}S_{27}X_3$ by Rietveld refinements of XRD results. $Bi_{13}S_{18}Cl_2$, $Bi_{13}S_{18}Br_2$, and $Bi_{13}S_{18}I_2$ are indirect *n*-type semiconductors, displaying a strong and broad light absorption in the range from ultraviolet to near-IR light with narrow band gaps. Uniform $Bi_{13}S_{18}X_2$ thin films are fabricated using a facile physical vapor deposition (PVD) method for the fabrication of solar cells. The photovoltaic study demonstrates that $Bi_{13}S_{18}X_2$ compounds can be used as light absorbers for solar cells and photodetector devices. $Bi_{13}S_{18}Br_2$ exhibits the best photovoltaic performance in $Bi_{13}S_{18}X_2$ compounds. This work provides important insights for the development of nontoxic and low-cost $Bi_{13}S_{18}X_2$-based solar cells.

II. EXPERIMENTAL SECTION

A. Chemicals and reagents

Hydroiodic acid (HI, 57% in water), hydrobromic acid (HBr, 48% in water), methylamine solution (CH_3NH_2, 40% in water), $BiBr_3$ (98%), and BiI_3 (98%) are purchased from Sigma-Aldrich. CH_4N_2S (99.0%) is purchased from TCI Chemicals and $BiCl_3$ (99.0%), ethylene glycol, and acetone are purchase from Wako Chemicals. All chemicals and reagents are analytical grade and used as received.

B. Synthesis of bismuth chalcogenide halide powder samples

CH_3NH_3I is synthesized by the reaction of methylamine (24 ml) with HI solution (10 ml) at 0 °C for 2 h in a rotary evaporator at 120 rpm and then evaporated at 80 °C. The precipitate is washed three times with ethanol and then diethyl ether at room temperature and dried at 60 °C for 24 h. CH_3NH_3Br is synthesized by the reaction of methylamine (27.86 ml) with HBr solution (40 ml) by similar manner to the case of CH_3NH_3I. For the synthesis of $Bi_{13}S_{18}Br_2$ powder sample, $BiBr_3$ (2 mmol), CH_3NH_3Br (3 mmol), and CH_4N_2S (4 mmol) are solvothermally treated with 5 ml of ethylene glycol solvent in a Teflon-lined stainless-steel autoclave with 100 ml capacity at 200 °C for 12 h under stirring conditions. The $Bi_{13}S_{18}I_2$ sample is synthesized by the same method using BiI_3, CH_3NH_3I, and CH_4N_2S as starting materials at 195 °C. The $Bi_{13}S_{18}Cl_2$ sample is synthesized by solvothermal treatment of $BiCl_3$ (5 mmol) and CH_4N_2S (4 mmol) in 5 ml of acetone solvent at 200 °C for 12 h under stirring conditions. The obtained powder samples are filtered, washed

with ethanol or acetone, and dried in a drying oven at 60 °C for 12 h.

C. Fabrication of bismuth chalcogenide halide pellet samples

The synthesized bismuth chalcogenide halide powder samples are gently ground into fine powder. The powder samples are then pressed using a pellet press mold with a diameter of 10 mm at 30 MPa for 3 min. Subsequently, cold isostatic press (CIP) treatment is employed on the pellet sample with a pressure of 200 MPa for 5 min to increase sample density. The thickness of the pellets is controlled at about 1 mm.

D. Fabrication of TiO_2 electrode and $Bi_{13}S_{18}X_2$ films

The TiO_2 electrode is prepared in the following manner [35]. A fluorine-doped tin oxide (FTO) conducting glass plate is cleaned in distilled water and acetone by ultrasonication for 10 min, consecutively. Then the FTO glass plate is dipped in 0.1 M titanium tetraisopropoxide solution for 1 min and washed with distilled water and ethanol, dried at room temperature, and calcined at 480 °C for 1 h to coat the FTO glass surface with a dense TiO_2 thin film. A desired amount of $Bi_{13}S_{18}X_2$ bulk sample is transferred to a tungsten basket attached to copper feedthroughs inside a thermal evaporator (Vacuum Device, VE-2012). The TiO_2 electrode is placed at 7 cm below the tungsten basket. After a vacuum of 2×10^{-5} Pa is established, an electric current of 20 A is applied, and this is maintained for about 5 min evaporation time. Then, $Bi_{13}S_{18}X_2$-deposited TiO_2 electrodes are transferred to a furnace and heated under a N_2 atmosphere at a desired temperature for 12 h. The thickness of the $Bi_{13}S_{18}X_2$ thin film is estimated from the amount of $Bi_{13}S_{18}X_2$ added and the distance between the tungsten basket and the TiO_2 electrode. The broken $Bi_{13}S_{18}X_2$ pellet is used for the bulk sample.

E. Fabrication and characterization of solar cells

$Bi_{13}S_{18}X_2$-solar cells are comprised of the $Bi_{13}S_{18}X_2$-coated TiO_2 electrode as an anode, Pt-coated FTO glass as a cathode, and an electrolyte solution between the anode and the cathode. The electrolyte solution contains 0.1 M LiI, 0.01 M I_2, 0.6 M 1-butyl-3-*n*-propylimidazolium iodide, 0.4 M 4-*tert*-butylpyridine, and 0.1 M guanidine thiocyanate in a mixed solvent of acetonitrile and valeronitrile (Vol.-Vol. = 85:15). The photocurrent-voltage characteristic curves for the $Bi_{13}S_{18}X_2$-based solar cells are measured using a Hokuto-Denko BAS100B electrochemical analyzer under irradiation with AM1.5 simulated sunlight (100 mW/cm^2), using a sunlight simulator (Yamashita Denso, YSS-E40). A light-passing mask is fixed on the surface of the FTO glass of the anode to set the effective irradiation area on the cell at 0.25 cm^2.

F. Physical analysis

The crystal structures of the samples are investigated using a powder x-ray diffractometer (Shimadzu, model XRD-6100) with Cu $K\alpha$ ($\lambda = 0.1542$ nm) radiation. The FullProf software is used for the Rietveld refinement of structure. The morphologies of the samples are observed using field-emission scanning electron microscopy (FESEM; JEOL, ISM-7001F) and their chemical compositions are measured using an energy-dispersive x-ray spectrometer (EDX) attached to the FESEM at an accelerating voltage of 15 kV. Transmission electron microscopy (TEM) and high-resolution TEM (HRTEM) observations are performed on a JEOL model JEM-3010 system at 300 kV. Atomic force microscope (AFM) images are acquired in contact mode on a Dimensions Hybrid Nanoscope system (NanoTechnology, SPA-400/Nano Navi Station, SII). Mott-Schottky plots are measured using an electrochemical analyzer (Shanghai Chenhua, CHI660E). Ultraviolet–visible–near-infrared (UV-vis-NIR) absorption spectra are obtained on a Shimadzu SolidSpec-3700 UV-vis-NIR spectrophotometer at room temperature. The thermogravimetric differential thermal analysis (TGDTA) is carried out using a thermal analyzer (Shimadzu, DTG-60H) at a heating rate of 10 °C min^{-1}. For conductivity measurements, a voltage of 100 V is applied to the $Bi_{13}S_{18}X_2$ pellet samples, and the current is measured using a ferroelectric testing system (Toyo Corporation, FCE3-4KVSYS) at room temperature. X-ray photoelectron spectroscopy (XPS) is performed using a Kratos Axis Supra x-ray photoelectron spectrometer. The XPS spectra are calibrated to an adventitious carbon peak at 284.6 eV. All binding energy (BE) values are calibrated by the C 1s peaks at 284.6 eV of the surface adventitious carbon. Ultraviolet photoelectron spectroscopy (UPS) is carried out using a Thermo Fisher ESCALAB 250Xi with helium-lamp radiation (21.22 eV) as an excitation source, and Fermi level is calibrated with Au. The relationship of work function (Φ), lamp radiation ($h\nu$), second-electron cutoff energy (E_{cutoff}), and Fermi energy (E_F) can be illustrated by

$$\Phi = h\nu - (E_{\text{cutoff}} - E_F) \tag{1}$$

where $\Phi = E_{\text{vac}} - E_F$, with E_{vac} as the vacuum-level energy; therefore, E_F can be evaluated from $h\nu$ and E_{cutoff}. (Φ) [36].

III. RESULTS AND DISCUSSION

A. Synthesis and structure of bismuth chalcogenide halide compounds

In our previous study, we developed a solvothermal reaction system of BiI_3, CH_4N_2S, and CH_3NH_3I in ethylene glycol solvent for the synthesis of $Bi_{13}S_{18}I_2$ [27]. In the present study, a solvothermal reaction system

of $BiBr_3$, CH_4N_2S, and CH_3NH_3Br in ethylene glycol solvent is used for the synthesis of $Bi_{13}S_{18}Br_2$ and a solvothermal reaction system of $BiCl_3$ and CH_4N_2S in acetone solvent is used for the synthesis of $Bi_{13}S_{18}Cl_2$. The $Bi_{13}S_{18}Br_2$ and $Bi_{13}S_{18}Cl_2$ samples with high purity and high crystallinity can be obtained by solvothermal treatments of a mixture of $BiBr_3$, CH_4N_2S, and CH_3NH_3Br in ethylene glycol with molar ratios of 2:4:3 $BiBr_3/CH_4N_2S/CH_3NH_3Br$ at 200 °C for 12 h and a mixture of $BiCl_3$ and CH_4N_2S in acetone with a molar ratio of 5:4 of $BiCl_3/CH_4N_2S$ at 200 °C for 12 h. The detailed synthesis results for $Bi_{13}S_{18}Br_2$ and $Bi_{13}S_{18}Cl_2$ by the solvothermal reactions are provided in the Supplemental Material [37]. A $Bi_{13}S_{18}I_2$ sample is synthesized by solvothermal treatment of a mixture of BiI_3, CH_4N_2S, and CH_3NH_3I in ethylene glycol with molar ratios of 2:4:3 of $BiBr_3/CH_4N_2S/CH_3NH_3Br$ at 195 °C for 12 h. The $Bi_{13}S_{18}Br_2$ and $Bi_{13}S_{18}Cl_2$ samples have a fibrous particle morphology similar to that of $Bi_{13}S_{18}I_2$ (Fig. S5 within the Supplemental Material [37]) [27]. The TGDTA results reveal that the thermostabilities of $Bi_{13}S_{18}X_2$ increase in the order of $Bi_{13}S_{18}I_2 < Bi_{13}S_{18}Cl_2 < Bi_{13}S_{18}Br_2$ (Fig. S6 within the Supplemental Material [37]).

The structure of $Bi_{13}S_{18}I_2$ was initially reported as a hexagonal system with the $P6_3$ space group and compositional formula of $Bi(Bi_2S_3)_9I_3$ in 1971 [31]. Thereafter, some studies also reported that $Bi_{13}S_{18}I_2$ belonged to a hexagonal system with the $P6_3/m$ or $P6_3$ space groups and compositional formula of $Bi_{19}S_{27}I_3$, which is the same as that of $Bi(Bi_2S_3)_9I_3$, where all Bi are trivalent Bi(III) [25,32,33,38]. Recently, Groom *et al.* rediscovered the structure by studying a single crystal and proved a hexagonal system with the $P3$ space group, rather than $P6_3$ or $P6_3/m$, and a compositional formula of $Bi_{13}S_{18}I_2$, rather than $Bi_{19}S_{27}I_3$. Bi(III) and Bi(II) coexist in $Bi_{13}S_{18}I_2$ as $(Bi^{3+})_{12}(Bi_2^{4+})_{0.5}(L^{2-})_{18}(I^-)_2$, where a bivalent Bi(II) dimer of Bi_2^{4+} is formed [22]. Kramer reported $Bi_{13}S_{18}Br_2$ with a structure similar to that of $Bi_{13}S_{18}I_2$: a hexagonal system with the $P6_3$ space group and compositional formula of $Bi(Bi_2S_3)_9Br_3$ in 1976 [34]. $Bi_{13}S_{18}Br_2$, with the $P6_3/m$ space group and compositional formula of $Bi_{19}S_{27}Br_3$ has also been reported [28,29,39]. Only a few studies have been reported on $Bi_{13}S_{18}Cl_2$ and suggest that $Bi_{13}S_{18}Cl_2$ belongs to the hexagonal system with $P6_3$ or $P6_3/m$ space groups, similar to $Bi_{13}S_{18}Br_2$ [24,30,40]. We believe that the formation of the Bi(II) dimer (BI_2^{4+}) is also possible in $Bi_{13}S_{18}Br_2$ and $Bi_{13}S_{18}Cl_2$, similar to $Bi_{13}S_{18}I_2$. Therefore, the $P3$ space group and compositions of $(Bi^{3+})_{12}(Bi_2^{4+})_{0.5}(S^{2-})_{18}(X^-)_2$ (X = Br and Cl) are also possible, which has inspired us to refine the structures of $Bi_{13}S_{18}X_2$.

The structures of $Bi_{13}S_{18}X_2$ are refined by using the Rietveld profile refinement method for two space groups, $P3$ and $P6_3$, and the results are shown in Table I for the $P3$ space group and Table S1 within the Supplemental Material [37] for the $P6_3$ space groups. Since fractional atomic coordinates for $Bi_{13}S_{18}Br_2$ and $Bi_{13}S_{18}Cl_2$ with the $P6_3/m$ space group have not been reported, $P6_3/m$ is not used in the structural refinements. The structure models for $Bi_{13}S_{18}Br_2$ and $Bi_{13}S_{18}Cl_2$ with the $P3$ space group are built on the basis of the fractional atomic coordinates of $Bi_{13}S_{18}I_2$ by substituting I^- lattice positions with Br^- and Cl^-, respectively, because the fractional atomic coordinates for $Bi_{13}S_{18}Cl_2$ and $Bi_{13}S_{18}Br_2$ with the $P3$ space group are not included in the crystal structure database. Rietveld refinement results reveal that the $P3$ space group give much lower weighted profile residual errors (R_{WP}) and expected weighted profile factor (R_{exp}) for $Bi_{13}S_{18}Cl_2$, $Bi_{13}S_{18}Br_2$, and $Bi_{13}S_{18}I_2$ than those of the $P6_3$ space group. Overall the chi squared [$\chi^2=(R_{WP}/R_{exp})^2$] are 1.550, 1.910, and 1.402 for $Bi_{13}S_{18}Cl_2$, $Bi_{13}S_{18}Br_2$, and $Bi_{13}S_{18}I_2$ with the $P3$ space group, respectively. The small R_{WP} and R_p values correspond high quality of the refinement fitting results [41]. Usually, the Rietveld refinement results are reliable when $R_{WP} < 10\%$ and χ^2 is between 1 and 2% [42]. Therefore, we can conclude that the structures of $Bi_{13}S_{18}X_2$ belong to the hexagonal system with the $P3$ space group of because the R values for the $P3$ space group are lower than those for the $P6_3$ space group and satisfy that conditions of $R_{WP} < 10\%$ and $\chi^2 = 1$–2%.

TABLE I. Refined structural parameters and R factors for $Bi_{13}S_{18}X_2$ using the $P3$ space group.

Formula	Lattice parameters	Cell volume (Å^3)	R factors (%)	χ^2
$Bi_{13}S_{18}Cl_2$	$a = b = 15.4081(4)$ $c = 4.0128(1)$ $\alpha = \beta = 90°, \gamma = 120°$	825.058(48)	$R_{WP} = 9.921$ $R_p = 6.362$ $R_{exp} = 7.661$	1.550
$Bi_{13}S_{18}Br_2$	$a = b = 15.5074(1)$ $c = 4.0130(1)$ $\alpha = \beta = 90°, \gamma = 120°$	835.759(50)	$R_{WP} = 8.390$ $R_p = 6.160$ $R_{exp} = 4.370$	1.910
$Bi_{13}S_{18}I_2$	$a = b = 15.6421(1)$ $c = 4.0205(1)$ $\alpha = \beta = 90°, \gamma = 120°$	851.935(14)	$R_{WP} = 9.052$ $R_p = 6.794$ $R_{exp} = 6.458$	1.402

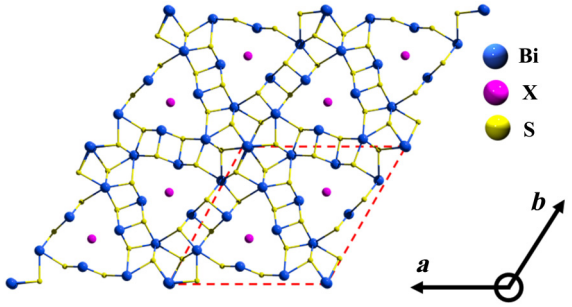

FIG. 1. Structure of hexagonal $Bi_{13}S_{18}X_2$ with $P3$ space group.

The Rietveld fitting results using the $P3$ space group of are shown in Fig. S8 within the Supplemental Material [37]. The plots of differences between XRD data and refined results indicate excellent fitting using the $P3$ space group.

Based on the structure refinement results, we believe that the structures of $Bi_{13}S_{18}X_2$ compounds belong to a hexagonal system with the $P3$ space group and a chemical formula of $Bi_{13}S_{18}X_2$, as shown in Fig. 1. This structure is interesting, in which a unique triangular tunnel structure is formed by $[Bi_4S_6]$-ribbon spokes in the c-axial direction, X^- are located in the tunnel sites, and Bi(II) dimers of Bi_2^{4+} are located at the hexagonal center. The TEM and HRTEM results suggest that fibrous $Bi_{13}S_{18}Br_2$ and $Bi_{13}S_{18}Cl_2$ particles are single crystals, which grow in the c-axial direction, namely, the tunnel direction (Fig. S9 within the Supplemental Material [37]). The refined structural parameters, including the atomic positions, are provided in Tables S2–S4 within the Supplemental Material [37].

B. Photoelectric behavior of bismuth chalcogenide halide compounds

Pellets of $Bi_{13}S_{18}X_2$ are used for the conductivity measurements at room temperature (Fig. S10 within the Supplemental Material [37]). The electrical conductivity (σ) is calculated from the applied voltage (V), measured current (I), thickness of the pellet (L), and area (S) of the pellet sample:

$$\sigma = \frac{IL}{VS}. \tag{2}$$

The calculated electrical conductivities of the $Bi_{13}S_{18}Cl_2$, $Bi_{13}S_{18}Br_2$, and $Bi_{13}S_{18}I_2$ pellet samples are 1.07×10^{-5}, 2.58×10^{-6}, and 8.85×10^{-7} S·cm^{-1}, respectively. We can see that the electrical conductivity decreases in the order of $Bi_{13}S_{18}Cl_2 > Bi_{13}S_{18}Br_2 > Bi_{13}S_{18}I_2$ by around 1 order of magnitude with increases of the atomic radius of halogen. It has been reported that the conductivity of the $Bi_{13}S_{18}I_2$ single crystal is 9×10^{-4} S cm^{-1}, which is much higher than the value of the pellet sample of the present study [21]. This may be due to the large resistance between grain boundaries for the polycrystalline pellet sample [43,44]. However, there are no reports on the electrical conductivities of $Bi_{13}S_{18}Cl_2$ and $Bi_{13}S_{18}Br_2$. We can speculate that single crystals of $Bi_{13}S_{18}Cl_2$ and $Bi_{13}S_{18}Br_2$ possess higher electrical conductivities than those of the polycrystalline pellet samples reported here. The cross-section FESEM images of $Bi_{13}S_{18}X_2$ pellets show similar morphologies and comparable densities (Fig. S11 within the Supplemental Material [37]). The large difference in electrical conductivities of $Bi_{13}S_{18}X_2$ pellet samples should be attributed to intrinsic effects caused by different halogens.

The $Bi_{13}S_{18}X_2$ samples are black crystals, meaning a broad absorption in the visible-light range. UV-vis-NIR absorption spectroscopy is employed to study their optical properties (Fig. 2). $Bi_{13}S_{18}Cl_2$, $Bi_{13}S_{18}Br_2$, and $Bi_{13}S_{18}I_2$ show very similar absorption spectra; two strong broad absorption bands at around 700 nm in the visible-light range and at 1100 nm in the near-IR wavelength range are observed [Fig. 2(a)]. A slightly redshifted absorption edge and a gradually increasing absorption intensity are observed with increasing atomic radius of halogen.

Since only limited studies have been reported on $Bi_{13}S_{18}X_2$ compounds, there is debate about their band gaps. Wu *et al.* reported a direct transition band gap of 1.6 eV for $Bi_{13}S_{18}Cl_2$ calculated from the first strong cutoff in the visible-light range [30]. Similarly, Deng *et al.* also obtain a direct transition band gap of 1.42 eV for $Bi_{13}S_{18}Br_2$ from the first strong cutoff in the visible-light range [28]. Differently, Ho *et al.* reported an indirect transition band gap of 0.73 eV and a direct transition band gap of 1.08 eV for $Bi_{13}S_{18}I_2$ based on transmittance and thermoreflectance measurements, respectively [21]. Groom *et al.* rediscovered $Bi_{13}S_{18}I_2$ by studying a single crystal and combined the results with electronic structure calculations, to obtain an indirect transition band gap of 0.82 eV from the second strong cutoff in the NIR range [22]. These results suggest that the first strong cutoff in the visible-light range is a direct transition and the second strong cutoff in the NIR range is an indirect transition.

The band-gap energy (E_g) of a semiconductor can be estimated using Tauc's formula, $(Ahv)^{1/n} = B(hv-E_g)$, where A, B, and hv are the absorption coefficient, a constant, and the incident photon energy, respectively, and the exponent n is equal to 1/2 or 2 for the allowed direct or indirect transition, respectively [45]. Tauc's formula can be represented as the transformed Kubelka-Munk function, $(Ahv)^{1/2} = C(hv-E_g)$, for the indirect transition and $(Ahv)^2 = C(hv-E_g)$ for the direct transition [46]. The band-gap energy of the second strong cutoff in the NIR range for $Bi_{13}S_{18}X_2$ can be estimated from the transformed Kubelka-Munk function versus the photon energy [Fig. 2(b)]. The estimated indirect transition band-gap energies of $Bi_{13}S_{18}Cl_2$, $Bi_{13}S_{18}Br_2$, and $Bi_{13}S_{18}I_2$ samples

are 0.76, 0.80, and 0.81 eV, respectively. These results are close to the band-gap energy of $Bi_{13}S_{18}I_2$ reported by Groom *et al.* [22]. In addition, plots of $(Ahv)^2$ versus the photon energy for the first strong cutoff in the visible-light range are shown in Fig. S12 within the Supplemental Material [37], exhibiting similar direct transition band-gap energies of 1.34, 1.32, and 1.30 eV for $Bi_{13}S_{18}Cl_2$, $Bi_{13}S_{18}Br_2$, and $Bi_{13}S_{18}I_2$, respectively.

The band structure, Fermi level, and work function are very important parameters for photoelectric materials [36]. The Fermi level and valence-band maxima (VBMs) of $Bi_{13}S_{18}X_2$ are examined by using UPS. The $Bi_{13}S_{18}X_2$ samples show similar UPS spectra with second-electron cutoff energies (E_{cutoff}) of 17.77, 17.50, and 17.25 eV for $Bi_{13}S_{18}Cl_2$, $Bi_{13}S_{18}Br_2$, and $Bi_{13}S_{18}I_2$, respectively, as shown in Fig. 3(a). The Fermi levels of $Bi_{13}S_{18}Cl_2$, $Bi_{13}S_{18}Br_2$, and $Bi_{13}S_{18}I_2$ can be evaluated as −3.97, −3.72, and −3.45 eV, respectively, from Eq. (1). The inset of Fig. 3(a) shows an enlargement of UPS spectra near the Fermi edge; the VBMs of $Bi_{13}S_{18}Cl_2$, $Bi_{13}S_{18}Br_2$, and

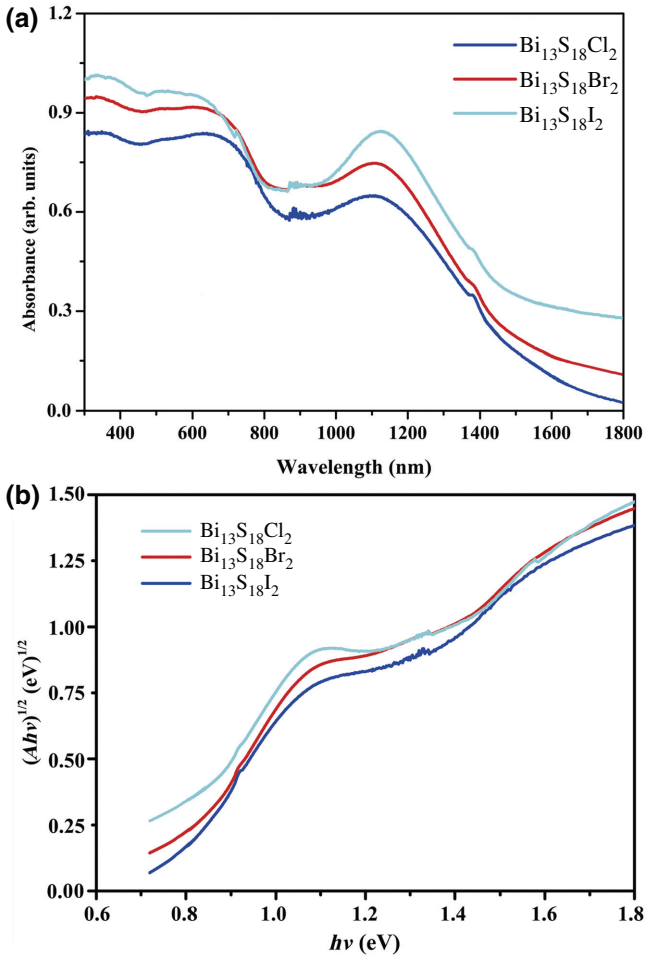

FIG. 2. (a) UV-vis-NIR absorption spectra and (b) corresponding plots of the transformed Kubelka-Munk function versus hv of $Bi_{13}S_{18}X_2$ powder samples.

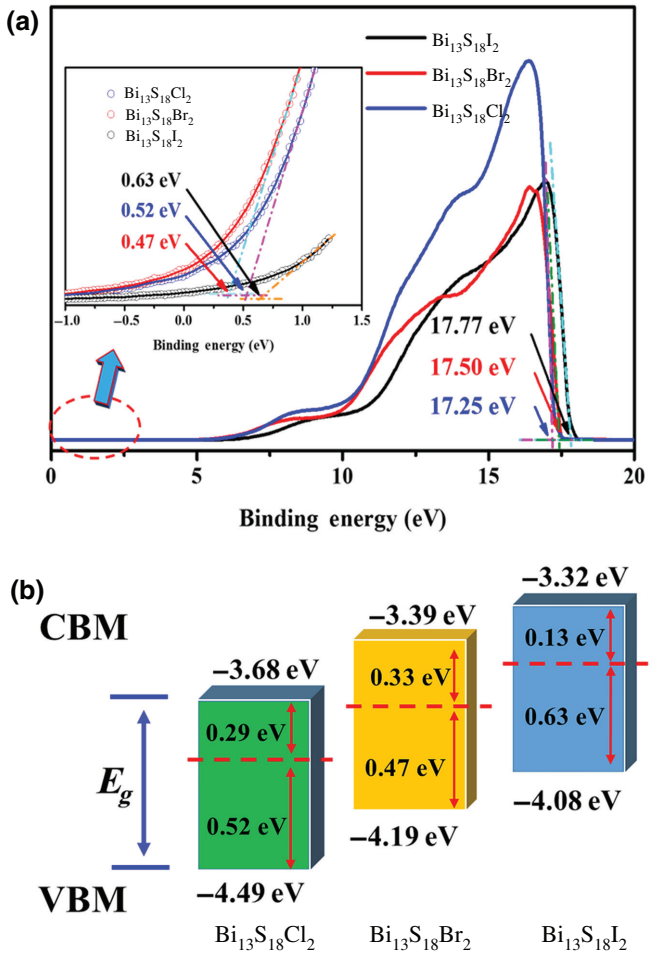

FIG. 3. (a) UPS spectrum of $Bi_{13}S_{18}X_2$ and (b) energy-band structures of $Bi_{13}S_{18}X_2$. Inset in (a) shows an enlargement of red-circled part.

$Bi_{13}S_{18}I_2$ are located at 0.52, 0.47, and 0.63 eV below the Fermi level, respectively. Therefore, the conduction-band minima (CBMs) will be located at 0.29, 0.33, and 0.13 eV above the Fermi level for $Bi_{13}S_{18}Cl_2$, $Bi_{13}S_{18}Br_2$, and $Bi_{13}S_{18}I_2$, respectively, as their band gaps (E_g) are 0.76, 0.80, and 0.81 eV, respectively, Therefore, we can give the energy-band structures for $Bi_{13}S_{18}X_2$, as shown in Fig. 3(b).

The VBMs for $Bi_{13}S_{18}Cl_2$ and $Bi_{13}S_{18}Br_2$ are also examined from their valence-band XPS spectra, as shown in Fig. S13 within the Supplemental Material [37]. The VBMs are located at 0.52 and 0.48 eV below the Fermi level for $Bi_{13}S_{18}Cl_2$ and $Bi_{13}S_{18}Br_2$, respectively, which are very close to the results of UPS spectra. $Bi_{13}S_{18}Cl_2$ and $Bi_{13}S_{18}Br_2$ should also be an *n*-type semiconductor like $Bi_{13}S_{18}I_2$ because their Fermi levels are close to the conduction-band minimum [27,47]. The results of the Mott-Schottky plot also prove that $Bi_{13}S_{18}Cl_2$, $Bi_{13}S_{18}Br_2$, and $Bi_{13}S_{18}I_2$ are *n*-type semiconductors (Fig. S14 within the Supplemental Material [37]). The *n*-type

semiconductor shows a positive slope value and p-type semiconductor shows a negative slope value in the Mott-Schottky plot [48]. The positive slope values of $Bi_{13}S_{18}X_2$ suggest they are n-type semiconductors.

The surface valences state and chemical compositions of the $Bi_{13}S_{18}Cl_2$ and $Bi_{13}S_{18}Br_2$ samples are examined by XPS. The XPS survey spectra reveal the predominant presence of sulfur, bismuth, and chlorine for $Bi_{13}S_{18}Cl_2$ and sulfur, bismuth, and bromine for $Bi_{13}S_{18}Br_2$; all of the $Bi_{13}S_{18}X_2$ samples present small amounts of carbon and oxygen impurities (Fig. S15 within the Supplemental Material [37]). Carbon and oxygen should originate from the residual organic precursor and adsorbed oxygen or water molecules on the particle surface. The Bi $4f_{7/2}$ and Bi $4f_{5/2}$ peaks are observed at 158.0 and 163.3 eV for $Bi_{13}S_{18}Cl_2$ and 157.9 and 163.2 eV for $Bi_{13}S_{18}Br_2$; these values corresponds to those of 158.0 and 163.3 eV for $Bi_{13}S_{18}I_2$ [27]. Notably, the observed chemical-shift values of Bi $4f$ for $Bi_{13}S_{18}X_2$ are little different (about 0.7 eV) from trivalent Bi(III) of 158.7 and 164.0 eV in BiSI [27,49]. This difference should be attributed to the coexistence of bivalent Bi(II) and trivalent Bi(III) in $Bi_{13}S_{18}X_2$, but only trivalent Bi(III) in BiSI. The XPS results support our structural study results that $Bi_{13}S_{18}X_2$ should adopt a structure with the $P3$ space group and chemical formula of $(Bi^{3+})_{12}(Bi_2^{4+})_{0.5}(S^{2-})_{18}(X^-)_2$ ($Bi_{13}S_{18}X_2$) with bivalent dimers (Bi_2^{4+}), rather than the $P6_3$ space group and chemical formulas of $Bi_{19}S_{27}X_3$ or $[Bi(Bi_2S_3)_9X_3]_{2/3}$. Single peaks of S $2s$ are observed at 225.1 and 225.2 eV for $Bi_{13}S_{18}Cl_2$ and $Bi_{13}S_{18}Br_2$, respectively. The Cl $3p_{3/2}$ and Cl $3p_{5/2}$ spin-orbit components are observed at 199.0 and 197.4 eV for $Bi_{13}S_{18}Cl_2$, respectively. The two peaks located at 68.8 and 67.8 eV can be attributed to Br $3d_{3/2}$ and Br $3d_{5/2}$ spin-orbit components of Br^- in $Bi_{13}S_{18}Br_2$, respectively. The XPS quantitative analysis results suggest that the atomic ratios of X : Bi : S are 1:6.4:8.9 and 1:6.4:9.0 in the $Bi_{13}S_{18}Cl_2$ and $Bi_{13}S_{18}Br_2$ samples, respectively, which are very close to the stoichiometric molar ratio of 1:6.5:9.0 of $(Bi^{3+})_{12}(Bi_2^{4+})_{0.5}(S^{2-})_{18}(X^-)_2$, indicating the successful preparation of $Bi_{13}S_{18}Cl_2$ and $Bi_{13}S_{18}Br_2$ phases.

C. Fabrication of bismuth chalcogenide halide thin films by PVD process

Previously, we reported a study on a $Bi_{13}S_{18}I_2$ -based solar cell with a PCE of 0.85%, in which a $Bi_{13}S_{18}I_2$ thin film fabricated by a modified solvothermal process is used as a light absorber [27]. In the present study, a facile PVD process is developed for the fabrication of uniform $Bi_{13}S_{18}X_2$ thin films as light absorbers for $Bi_{13}S_{18}X_2$-based solar cells. Figure 4 shows the XRD patterns of as-prepared $Bi_{13}S_{18}Br_2$ film prepared by the PVD process and films obtained after heat treatment at different temperatures under a N_2 atmosphere for 12 h. The as-prepared

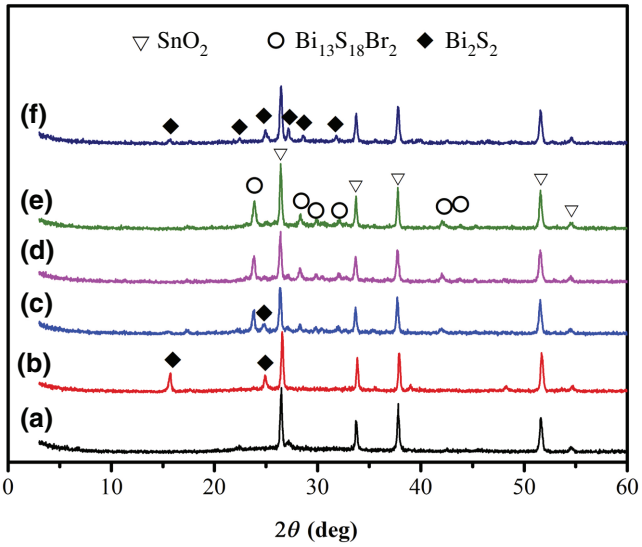

FIG. 4. XRD patterns of (a) as-prepared $Bi_{13}S_{18}Br_2$ film on FTO glass substrate by PVD process and film obtained after heat treatment at (b) 100, (c) 150, (d) 200, (e) 250, and (f) 300 °C under N_2 atmosphere for 12 h, respectively.

$Bi_{13}S_{18}Br_2$ thin film is an amorphous phase, where only diffraction peaks of the SnO_2 phase of FTO glass substrate are observed. With increasing heat-treatment temperature, the Bi_2S_3 phase is formed at 100 °C, $Bi_{13}S_{18}Br_2$ and Bi_2S_3 phases are formed at 150 °C, the $Bi_{13}S_{18}Br_2$ single phase is formed at 200 and 250 °C. The crystallinity of $Bi_{13}S_{18}Br_2$ increases with increasing heat-treatment temperature. At 300 °C, the $Bi_{13}S_{18}Br_2$ phase is decomposed to the Bi_2S_3 phase. The as-prepared $Bi_{13}S_{18}Br_2$ film has a uniform thickness, but low density with some small pores in the amorphous film [Fig. S16(a) within the Supplemental Material [37]]. After heat treatment at 250 °C, a $Bi_{13}S_{18}Br_2$ film with high density and high crystallinity is obtained [Fig. S16(b) within the Supplemental Material [37]]. The $Bi_{13}S_{18}Cl_2$ and $Bi_{13}S_{18}I_2$ thin films can also be fabricated by a process similar to that of $Bi_{13}S_{18}Br_2$, namely, heat treatment of the amorphous $Bi_{13}S_{18}Cl_2$ and $Bi_{13}S_{18}I_2$ thin films fabricated by a PVD process at 250 °C under a N_2 atmosphere (Fig. S17 within the Supplemental Material [37]).

Energy-dispersive x-ray spectroscopy (EDS) analysis is employed to confirm the chemical compositions of $Bi_{13}S_{18}X_2$ powder samples used for the PVD process, as-prepared $Bi_{13}S_{18}X_2$ films, and $Bi_{13}S_{18}X_2$ films after heat treatment at 250 °C under a N_2 atmosphere (Table S5 within the Supplemental Material [37]). The $Bi_{13}S_{18}X_2$ powder samples have chemical compositions close to those of the expected stoichiometric compositions of $Bi_{13}S_{18}X_2$. Furthermore, the chemical compositions of the as-prepared $Bi_{13}S_{18}X_2$ films and the heat-treated films are almost the same as their powder samples, namely, very close to their expected stoichiometric compositions. The nanostructures

of the heat-treated $Bi_{13}S_{18}X_2$ films at 250 °C are investigated by using TEM and HRTEM analyses. As shown in Fig. S18 within the Supplemental Material [37], the high-density films are constructed from close-packed $Bi_{13}S_{18}X_2$ granular nanocrystals. The crystal sizes of nanocrystals of $Bi_{13}S_{18}Cl_2$, $Bi_{13}S_{18}Br_2$, and $Bi_{13}S_{18}I_2$ are about 10, 20, and 15 nm, respectively. The polycrystalline selected-area electron diffraction patterns are observed for the $Bi_{13}S_{18}X_2$ films, which correspond to powder samples in Fig. S9 within the Supplemental Material [37]. However, the granular nanocrystal morphologies are different from their powder samples with fibrous crystal morphologies (Fig. S5 within the Supplemental Material [37]). The above results suggest that the transformation reactions from the amorphous $Bi_{13}S_{18}X_2$ phases to the crystalline $Bi_{13}S_{18}X_2$ phases are near *in situ* crystallization reactions. In other words, neighboring Bi, S, and X compositions react together to form $Bi_{13}S_{18}X_2$ nanocrystals, without long-distance diffusion for the formation of fibrous crystals.

D. Performances of $Bi_{13}S_{18}X_2$-based solar cells

To study solar-cell performance, FTO/TiO_2/$Bi_{13}S_{18}X_2$ electrodes are fabricated. A dense TiO_2 film is coated on the surface of FTO conducting glass substrate as a hole-blocking layer. Then, $Bi_{13}S_{18}X_2$ films with different thicknesses are deposited on the dense TiO_2 film surface through a PVD process before heat treatment at 250 °C for 12 h under a N_2 atmosphere. The $Bi_{13}S_{18}X_2$-based solar cells are constructed from the FTO/TiO_2/$Bi_{13}S_{18}X_2$ electrodes, an electrolyte solution of the I_3^-/I^- redox couple as a hole-transporting material, and Pt-coated FTO conducting glass as a counter electrode, as shown in Fig. 5(a). In the present study, we mainly focus on the effect of the thickness of the $Bi_{13}S_{18}X_2$ light-harvesting layer on the solar-cell performance because it is known that the thickness of the light-harvesting layer is one of the most importance factors for solar cells [50–52]. If the light-harvesting layer is too thin, it cannot harvest enough photons, resulting a low photocurrent. However, if the light-harvesting layer is too thick, it will hinder charge-carrier extraction due to its large resistance, leading to a high percentage of exciton recombination.

A series of FTO/TiO_2/$Bi_{13}S_{18}X_2$/ (I_3^-/I^- redox couple)/Pt devices are fabricated with different $Bi_{13}S_{18}X_2$ film thicknesses in the range of 100 to 500 nm. The solar-cell parameters of short-circuit current densities (J_{SC}), open-circuit voltages (V_{OC}), fill factor (FF), and PCE are plotted as a function of $Bi_{13}S_{18}X_2$ film thickness in Fig. 6. The J_{SC} value of the $Bi_{13}S_{18}Br_2$ -based solar cell increases, reaches a maximum value of 7.5 mA/cm^2 at around 400 nm, and then decreases with increasing $Bi_{13}S_{18}Br_2$ film thickness [Fig. 6(a)]. $Bi_{13}S_{18}Cl_2$ and $Bi_{13}S_{18}I_2$ also exhibit similar J_{SC} behavior, with a maximum J_{SC} value of around 350 nm. The maximum J_{SC} value increases in the order

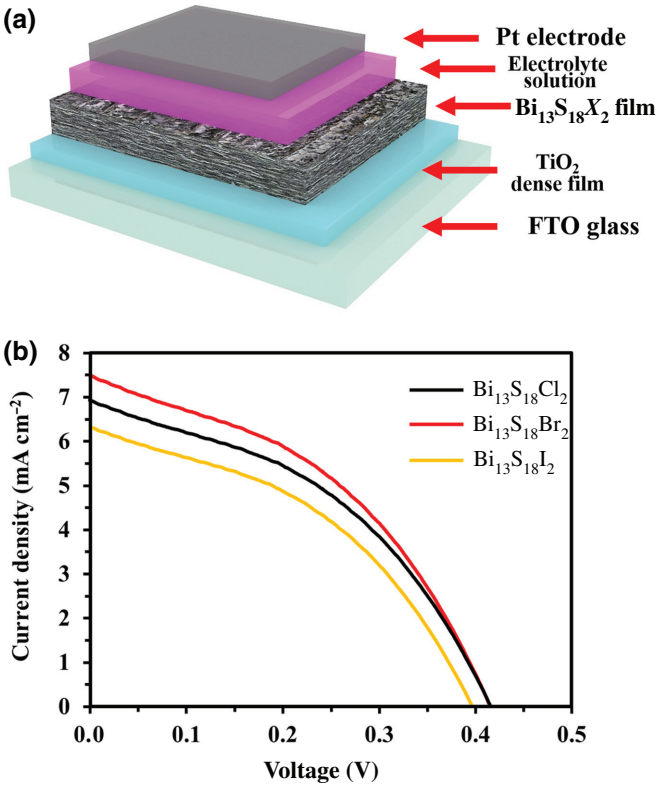

FIG. 5. (a) Schematic illustration of (a) $Bi_{13}S_{18}X_2$-based solar-cell structure and (b) J-V curve of $Bi_{13}S_{18}X_2$-based solar cells with optimum film thickness of $Bi_{13}S_{18}X_2$.

of $Bi_{13}S_{18}I_2 < Bi_{13}S_{18}Cl_2 < Bi_{13}S_{18}Br_2$. The V_{OC} values of $Bi_{13}S_{18}X_2$-based solar cells also increase, reach maximum values at around 350 nm, and then decrease with increasing $Bi_{13}S_{18}X_2$ film thickness [Fig. 6(b)]. However, the changes of V_{OC} values with changing the $Bi_{13}S_{18}X_2$ film thickness are much smaller than the those of J_{SC} values. The maximum V_{OC} values are 0.42, 0.42, and 0.38 V for $Bi_{13}S_{18}Cl_2$, $Bi_{13}S_{18}Br_2$, and $Bi_{13}S_{18}I_2$, respectively. These values are much smaller than the theoretical V_{OC} value of 0.9 V calculated from the conduction-band minimum of TiO_2 (−0.5 V) and the redox potential of I_3^-/I^- (0.4 V) for the hole-transporting material [53]. The FF values also exhibit similar behavior to that of V_{OC} values with maximum FF values of 33%, 35%, and 30% at $Bi_{13}S_{18}X_2$ film thicknesses of around 400 nm [Fig. 6(c)]. The FF values are quite low compared with those of high-performance solar cells.

The PCE values are mainly dependent on the J_{SC} values, that is, increase, reach maximum values at around 400 nm, and then decrease with increasing $Bi_{13}S_{18}X_2$ film thickness [Fig. 6(d)]. The maximum PCE value increases in the order of $Bi_{13}S_{18}I_2$ (0.75%) < $Bi_{13}S_{18}Cl_2$ (0.91%) < $Bi_{13}S_{18}Br_2$ (1.12%). The J-V curves and cell parameters of solar cells with optimum film thickness

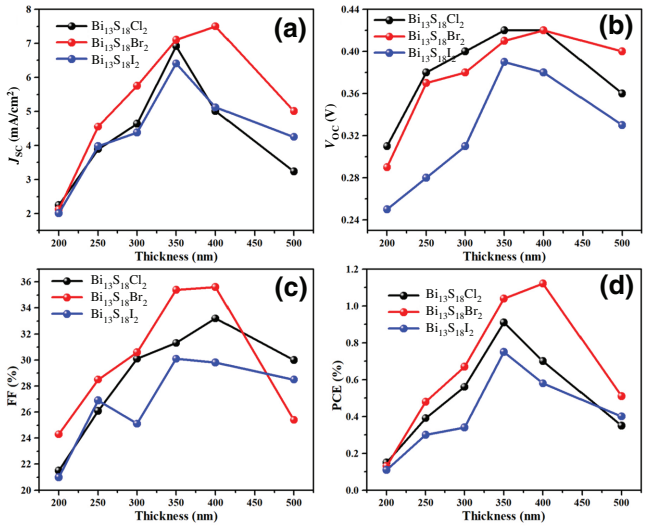

FIG. 6. (a) Short-circuit current density (J_{SC}), (b) open-circuit voltage (V_{OC}), (c) FF, and (d) PCE as a function of $Bi_{13}S_{18}X_2$ film thickness.

are shown in Fig. 5(b) and Table S6 within the Supplemental Material [37]. The PCE values increase in the order of $Bi_{13}S_{18}I_2 < Bi_{13}S_{18}Cl_2 < Bi_{13}S_{18}Br_2$, corresponding to the increase in J_{SC} values; in other words, PCEs are mainly dependent on J_{SC} values. Figure S19(a) within the Supplemental Material [37] shows the absorption spectra of the FTO/TiO_2/$Bi_{13}S_{18}X_2$ electrodes of the optimum devices after J-V current measurements. All of these three electrodes exhibit a broad light absorption in the wavelength range from 300 to 800 nm. The visible-light absorption increases in the order of $Bi_{13}S_{18}I_2 < Bi_{13}S_{18}Cl_2 < Bi_{13}S_{18}Br_2$, which corresponds with the increasing order of J_{SC} values of the $Bi_{13}S_{18}X_2$-based devices.

The optimum FTO/TiO_2/$Bi_{13}S_{18}Br_2$ electrode is investigated by FESEM and AFM (Fig. S20 within the Supplemental Material [37]). The as-prepared $Bi_{13}S_{18}Br_2$ film is constructed from nanoparticles and has a relatively smooth surface with some small pores [Fig. S20(a) within the Supplemental Material [37]], in which $Bi_{13}S_{18}Br_2$ is an amorphous phase [Fig. 4(a)]. The AFM image reveals a surface roughness of about 120 nm [Fig. S20(d) within the Supplemental Material [37]]. After heat treatment at 250 °C, the amorphous phase is transformed into the crystalline $Bi_{13}S_{18}Br_2$ phase, which accompanies an increase of the nanoparticle size and surface roughness to about 150 nm and disappearance of the small pores [Figs. S20(b) and (e) within the Supplemental Material [37]]. The surface roughness can enhance the light-scattering effect to improve the light absorption of the $Bi_{13}S_{18}Br_2$ film, resulting in an enlarged PCE [54]. The cross-section image of the FTO/TiO_2/$Bi_{13}S_{18}Br_2$ electrode reveals that the dense TiO_2 layer, with a thickness of about 50 nm, is coated tightly on the FTO surface and a $Bi_{13}S_{18}Br_2$ layer of high density, with a thickness of about 400 nm, coated tightly on the TiO_2 layer, which guarantees its high photoelectric performance. The results suggest that the PVD process developed in the present study is promising for the fabrication of high-performance $Bi_{13}S_{18}X_2$ films for solar cells. To confirm the device performance statistics, the J-V curves of five cells with the optimum film thickness are shown in Fig. S21 and the cell parameters are tabulated in Table S7 within the Supplemental Material [37], which display a narrow distribution in cell performance for $Bi_{13}S_{18}X_2$-based solar cells.

Compared with $Bi_{13}S_{18}I_2$-based solar cells prepared by a solvothermal process with cell parameters of PCE = 0.85%, J_{SC} = 3.82 mA/cm^2, V_{OC} = 0.58 V, and FF = 38.3%, the $Bi_{13}S_{18}I_2$ -based solar cell prepared by the PVD process possesses cell parameters of PCE = 0.75%, J_{SC} = 6.41 mA/cm^2, V_{OC} = 0.38 V, FF = 30%. The much higher J_{SC} value for the PVD process than that of the solvothermal process is due to the higher density and thickness of the $Bi_{13}S_{18}I_2$ film prepared by the PVD process, which enhances light harvesting. The higher V_{OC} and FF values for the solvothermal process can be attributed to the nanorod crystal morphology and thinner $Bi_{13}S_{18}I_2$ film prepared by the solvothermal process, which enhances the charge-carrier extraction by reducing the film resistance [20]. The results suggest that the PVD process developed in the present study is promising for the fabrication of a high-performance $Bi_{13}S_{18}X_2$ film for solar cells.

The cell performance of the $Bi_{13}S_{18}X_2$-based solar cells described above is still low. To further improve the cell performance, optimization of the solar cell is necessary. The $Bi_{13}S_{18}X_2$ compounds are indirect band-gap semiconductors. Compared with direct band-gap semiconductors, the lower light-absorption ability of the indirect band-gap semiconductors is a disadvantage as a light absorber for solar cells [55]. In other words, a thicker light-absorber layer is necessary for the solar cells using indirect band-gap semiconductors, which increases trap densities in the light-absorber layer. Silicon is an indirect band-gap semiconductor. The trap densities in silicon solar cells can be reduced by increasing the purity of silicon. Therefore, we believe that an improvement of the purities of the $Bi_{13}S_{18}X_2$ films will be effective at improving the performance of $Bi_{13}S_{18}X_2$-based solar cells. The results described above also suggest the possibility of the application of $Bi_{13}S_{18}X_2$ compounds as the light absorber for a near-infrared light photodetector device due to their photoelectric response in the wavelength region from the visible to near-infrared light.

IV. CONCLUSIONS

A solvothermal process is effective for the synthesis of high-quality stoichiometric $Bi_{13}S_{18}X_2$ compounds.

$Bi_{13}S_{18}X_2$ compounds adopt the same triangular tunnel structure of a hexagonal system with the *P*3 space group and composition of $(Bi^{3+})_{12}(B_2^{4+})_{0.5})(S^{2-})_{18}(X^-)_2$. The tunnel structure of $Bi_{13}S_{18}X_2$ is constructed from $[Bi_4S_6]$-ribbon spokes in the *c*-axial direction, X^- is located in the tunnel sites, and Bi(II) dimers of Bi_2^{4+} are located at the hexagonal center. $Bi_{13}S_{18}Cl_2$, $Bi_{13}S_{18}Br_2$, and $Bi_{13}S_{18}I_2$ compounds are indirect *n*-type semiconductors with narrow band gaps of 0.76, 0.80, and 0.81 eV, respectively, and exhibit strong light absorbance over a wide wavelength range from UV to NIR. The uniform $Bi_{13}S_{18}X_2$ films can be fabricated by using a combined process of PVD and heat treatment. Solar cells using $Bi_{13}S_{18}X_2$ light absorbers with a thickness of about 400 nm exhibit the highest PCEs of 0.91, 1.12, and 0.75% for $Bi_{13}S_{18}Cl_2$, $Bi_{13}S_{18}Br_2$, and $Bi_{13}S_{18}I_2$, respectively. The highest cell performance of $Bi_{13}S_{18}Br_2$ in $Bi_{13}S_{18}X_2$ can be attributed to its higher light-absorption ability. These results demonstrate the possible application of $Bi_{13}S_{18}X_2$ as stable light absorbers for solar-cell and photodetector devices, which can be fabricated by a facile PVD process.

ACKNOWLEDGMENTS

This work is supported by the Nippon Sheet Glass Foundation for Materials Science and Engineering, the Iwatani Naoji Foundation, and Grants-in-Aid for Scientific Research (B) (Grant No. 17H03458) from the Japan Society for the Promotion of Science.

[1] L. S. Gomez-Velazquez, A. Hernandez-Gordillo, M. J. Robinson, V. J. Leppert, S. E. Rodil, and M. Bizarro, The bismuth oxyhalide family: thin film synthesis and periodic properties, Dalton Trans. **47**, 12459 (2018).

[2] N. C. Miller and M. Bernechea, Research Update: Bismuth based materials for photovoltaics, APL Mater. **6**, 084503 (2018).

[3] J. L. DiMeglio and J. Rosenthal, Selective conversion of CO_2 to CO with high efficiency using an inexpensive bismuth-based electrocatalyst, J. Am. Chem. Soc. **135**, 8798 (2013).

[4] P. C. K. Vesborg and T. F. Jaramillo, Addressing the terawatt challenge: scalability in the supply of chemical elements for renewable energy, RSC Adv. **2**, 7933 (2012).

[5] C. Wadia, A. P. Alivisatos, and D. M. Kammen, Materials availability expands the opportunity for large-scale photovoltaics deployment, Environ. Sci. Technol. **43**, 2072 (2009).

[6] A. Audzijonis, L. Žigas, A. Kvedaravičius, and R. Žaltauskas, Origin of Ferroelectric Phase Transitions of $Bi_xSb_{1-x}SI$ Mixed Crystals, Ferroelectrics **392**, 45 (2009).

[7] D. Tiwari, F. Cardoso-Delgado, D. Alibhai, M. Mombrú, and D. J. Fermín, Photovoltaic Performance of Phase-Pure Orthorhombic BiSI Thin-Films, ACS Applied Energy Materials **2**, 3878 (2019).

[8] Y. Sasaki, Photoconductivity of a Ferroelectric Photoconductor BiSI, J. Appl. Phys. **4**, 614 (1965).

[9] A. Audzijonis, G. Gaigalas, L. Žigas, A. Pauliukas, R. Žaltauskas, A. Čerškus, D. Balnionis, and A. Kvedaravičius, Electronic structure of BiSeI clusters, J. Electron Spectrosc. Relat. Phenom. **164**, 19 (2008).

[10] J. Li, Y. Yu, and L. Zhang, Bismuth oxyhalide nanomaterials: layered structures meet photocatalysis, Nanoscale **6**, 8473 (2014).

[11] M. Guan, C. Xiao, J. Zhang, S. Fan, R. An, Q. Cheng, J. Xie, M. Zhou, B. Ye, and Y. Xie, Vacancy associates promoting solar-driven photocatalytic activity of ultrathin bismuth oxychloride nanosheets, J. Am. Chem. Soc. **135**, 10411 (2013).

[12] X. Zhang, Z. Ai, F. Jia, and L. Zhang, Generalized One-Pot Synthesis, Characterization, and Photocatalytic Activity of Hierarchical BiOX (X = Cl, Br, I) Nanoplate Microspheres, The Journal of Physical Chemistry C **112**, 747 (2008).

[13] J. Lee, B.-K. Min, I. Cho, and Y. Sohn, Synthesis and Characterization of 1-D BiSI and 2-D BiOI Nanostructures, Bull. Korean Chem. Soc. **34**, 773 (2013).

[14] H. Kunioku, M. Higashi, and R. Abe, Low-Temperature Synthesis of Bismuth Chalcohalides: Candidate Photovoltaic Materials with Easily, Continuously Controllable Band gap, Sci. Rep. **6**, 32664 (2016).

[15] K. Ren, J. Liu, J. Liang, K. Zhang, X. Zheng, H. Luo, Y. Huang, P. Liu, and X. Yu, Synthesis of the bismuth oxyhalide solid solutions with tunable band gap and photocatalytic activities, Dalton Trans. **42**, 9706 (2013).

[16] S. Bargozideh and M. Tasviri, Construction of a novel BiSI/MoS_2 nanocomposite with enhanced visible-light driven photocatalytic performance, New J. Chem. **42**, 18236 (2018).

[17] I. Aguiar, M. Mombrú, M. P. Barthaburu, H. B. Pereira, and L. Fornaro, Influence of solvothermal synthesis conditions in BiSI nanostructures for application in ionizing radiation detectors, Mater. Res. Express **3**, 025012 (2016).

[18] H. Shi, W. Ming, and M.-H. Du, Bismuth chalcohalides and oxyhalides as optoelectronic materials, Physical Review B **93**, 104108 (2016).

[19] A. M. Ganose, S. Matsumoto, J. Buckeridge, and D. O. Scanlon, Defect Engineering of Earth-Abundant Solar Absorbers BiSI and BiSeI, Chem. Mater. **30**, 3827 (2018).

[20] A. M. Ganose, K. T. Butler, A. Walsh, and D. O. Scanlon, Relativistic electronic structure and band alignment of BiSI and BiSeI: candidate photovoltaic materials, J. Mater. Chem. A **4**, 2060 (2016).

[21] C. H. Ho, Y. H. Chen, Y. K. Kuo, and C. W. Liu, The structure and opto-thermo electronic properties of a new $(Bi(Bi_2S_3)_9I_3)_{2/3}$ hexagonal nano-/micro-rod, Chem Commun (Camb) **53**, 3741 (2017).

[22] R. Groom, A. Jacobs, M. Cepeda, R. Drummey, and S. E. Latturner, $Bi_{13}S_{18}I_2$: (Re)discovery of a Subvalent Bismuth Compound Featuring $[Bi_2]_{4+}$ Dimers Grown in Sulfur/Iodine Flux Mixtures, Chem. Mater. **29**, 3314 (2017).

[23] K. Mariolacos, Single crystal synthesis of higher-order sulfohalogenides in the temperature gradient: $Bi_{19}S_{27}Br_3$, $Bi_2Cu_3S_4Br$, $Pb_{1-x}Bi_{2+x}Cu_{4-x}S_5I_2$, Mater. Res. Bull. **39**, 591 (2004).

[24] V. Kramer, Synthesis and Crystal Date of the Bismuth Sulphide Chloride $Bi_{19}S_{27}Cl_3$, Naturforsch **29b**, 688 (1974).

[25] Y. Yan, Y. Xu, S. Lei, X. Ou, L. Chen, J. Xiong, Y. Xiao, and B. Cheng, Fabrication of $Bi_{19}S_{27}I_3$ nanorod cluster films for enhanced photodetection performance, Dalton Trans. **47**, 3408 (2018).

[26] Y. Wu, H. Pan, X. Zhou, M. Li, B. Zhou, C. Yang, W. H. Zhang, J. Jie, and C. Li, Shape and composition control of $Bi_{19}S_{27}(Br_{3-x},I_x)$ alloyed nanowires: the role of metal ions, Chem. Sci. **6**, 4615 (2015).

[27] S. Li, L. Xu, X. Kong, T. Kusunose, N. Tsurumachi, and Q. Feng, Bismuth chalcogenide iodides $Bi_{13}S_{18}I_2$ and BiSI: solvothermal synthesis, photoelectric behavior, and photovoltaic performance, J. Mater. Chem. C **8**, 3821 (2020).

[28] C. Deng, H. Guan, and X. Tian, Novel $Bi_{19}S_{27}Br_3$ superstructures: facile microwave-assisted aqueous synthesis and their visible light photocatalytic performance, Mater. Lett. **108**, 17 (2013).

[29] Y. Chen, G. Tian, T. Feng, W. Zhou, Z. Ren, T. Han, Y. Xiao, and H. Fu, Single-crystalline $Bi_{19}Br_3S_{27}$ nanorods with an efficiently improved photocatalytic activity, CrystEngComm **17**, 6120 (2015).

[30] Z. Wu, Y. Jiang, X. Xiong, S. Ding, Y. Shi, X. Liu, Y. Liu, Z. Huang, and J. Hu, Synthesis and characterization of single-crystalline $Bi_{19}Cl_3S_{27}$ nanorods, Catal. Sci. Technol. **7**, 3464 (2017).

[31] G. Miehe and V. Kupčík, Die Kristallstruktur des $Bi(Bi_2S_3)_9J_3$, Die Naturwissenschaften **58**, 219 (1971).

[32] G. Shen, D. Chen, K. Tang, L. Huang, and Y. Qian, Large-scale synthesis of $(Bi(Bi_2S_3)_9I_3)_{0.667}$ submicrometer needle-like crystals via a novel polyol route, J. Cryst. Growth **249**, 331 (2003).

[33] Z. S. Aliev, S. S. Musayeva, F. Y. Jafarli, I. R. Amiraslanov, A. V. Shevelkov, and M. B. Babanly, The phase equilibria in the Bi–S–I ternary system and thermodynamic properties of the BiSI and $Bi_{19}S_{27}I_3$ ternary compounds, J. Alloys Compd. **610**, 522 (2014).

[34] V. Kramer, Crystal Data on Bismuth Sulphide, $Bi_{19}S_{27}Br_3$, J. Appl. Crystallogr. **6**, 499 (1973).

[35] C. Chen, L. Xu, G. A. Sewvandi, T. Kusunose, Y. Tanaka, S. Nakanishi, and Q. Feng, Microwave-Assisted Topochemical Conversion of Layered Titanate Nanosheets to {010}-Faceted Anatase Nanocrystals for High Performance Photocatalysts and Dye-Sensitized Solar Cells, Cryst. Growth Des. **14**, 5801 (2014).

[36] A. Kahn, Fermi level, work function and vacuum level, Mater. Horiz. **3**, 7 (2016).

[37] See the Supplemental Material at http://link.aps.org/supplemental/10.1103/PhysRevApplied.15.034040 for synthesis results for $Bi_{13}S_{18}Br_2$ and $Bi_{13}S_{18}Cl_2$.

[38] E. Makovicky, Cyclically twinned sulphosalt structures and their approximate analogues, Zeitschrift für Kristallographie **173**, 1 (1985).

[39] K. Mariolacos, The Crystal Structure of $Bi(Bi_2S_3)_9Br_3$, J. Appl. Crystallogr. **B32**, 1947 (1975).

[40] Z. Wu, Y. Liu, S. Zhang, Z. Huang, Q. Jiang, T. Zhou, and J. Hu, Biomimetic structure design and construction of cactus-like $MoS_2/Bi_{19}Cl_3S_{27}$ photocatalysts for efficient hydrogen evolution, J. Mater. Chem. A **6**, 21404 (2018).

[41] L. B. McCusker, R. B. Von Dreele, D. E. Cox, D. Louer, and P. Scardi, Rietveld refinement guidelines, J. Appl. Crystallogr. **32**, 36 (1999).

[42] B. H. Toby, R factors in Rietveld analysis: How good is good enough?, Powder Diffr. **21**, 67 (2012).

[43] S. Sharifi-Asl, V. Yurkiv, A. Gutierrez, M. Cheng, M. Balasubramanian, F. Mashayek, J. Croy, and R. Shahbazian-Yassar, Revealing Grain-Boundary-Induced Degradation Mechanisms in Li-Rich Cathode Materials, Nano Lett. **20**, 1208 (2020).

[44] L. Dai, H. Li, H. Hu, and S. Shan, Experimental study of grain boundary electrical conductivities of dry synthetic peridotite under high-temperature, high-pressure, and different oxygen fugacity conditions, J. Geophys. Res. **113**, B12211 (2008).

[45] J. Tauc, Optical properties and electronic structure of amorphous Ge and Si, Mater. Res. Bull. **3**, 37 (1968).

[46] M. A. Butler, Photoelectrolysis and physical properties of the semiconducting electrode WO_2, J. Appl. Phys. **48**, 1914 (1977).

[47] J. You, Z. Hong, Y. M. Yang, Q. Chen, M. Cai, T. B. Song, C. C. Chen, S. Lu, Y. Liu, H. Zhou, and Y. Yang, Low-temperature solution-processed perovskite solar cells with high efficiency and flexibility, ACS Nano **8**, 1674 (2014).

[48] A. W. Bott, Electrochemistry of Semiconductors, Curr. Sep. **17**, 87 (1998).

[49] J. Grigas, E. Talik, M. Adamiec, V. Lazauskas, and V. Nelkinas, XPS and electronic structure of quasi-one-dimensional BiSI crystals, J. Electron Spectrosc. Relat. Phenom. **153**, 22 (2006).

[50] D. Liu, M. K. Gangishetty, and T. L. Kelly, Effect of $CH_3NH_3PbI_3$ thickness on device efficiency in planar heterojunction perovskite solar cells, J. Mater. Chem. A **2**, 19873 (2014).

[51] L. C. Andreani, A. Bozzola, P. Kowalczewski, M. Liscidini, and L. Redorici, Silicon solar cells: toward the efficiency limits, Advances in Physics: X **4**, 1548305 (2018).

[52] Y. Sun, S. Lin, W. Li, S. Cheng, Y. Zhang, Y. Liu, and W. Liu, Review on Alkali Element Doping in Cu(In,Ga)Se_2 Thin Films and Solar Cells, Engineering **3**, 452 (2017).

[53] G. A. Sewvandi, Z. Tao, T. Kusunose, Y. Tanaka, S. Nakanishi, and Q. Feng, Modification of TiO_2 electrode with organic silane interposed layer for high-performance of dye-sensitized solar cells, ACS Appl. Mater. Interfaces **6**, 5818 (2014).

[54] L. Zheng, Y. Ma, S. Chu, S. Wang, B. Qu, L. Xiao, Z. Chen, Q. Gong, Z. Wu, and X. Hou, Improved light absorption and charge transport for perovskite solar cells with rough interfaces by sequential deposition, Nanoscale **6**, 8171 (2014).

[55] S. S. Iyer and Y. H. Xie, Light Emission from Silicon, Science **260**, 40 (1993).